HHS Public Access

Author manuscript

Neurobiol Dis. Author manuscript; available in PMC 2024 April 09.

Published in final edited form as:

Neurobiol Dis. 2024 March ; 192: 106414. doi:10.1016/j.nbd.2024.106414.

PAD2 dysregulation and aberrant protein citrullination feature prominently in reactive astrogliosis and myelin protein aggregation in sporadic ALS

Issa O. Yusuf[a], **Sepideh Parsi**[a,b], **Lyle W. Ostrow**[c], **Robert H. Brown**[d], **Paul R. Thompson**[a,e], **Zuoshang Xu**[a,*]

[a]Department of Biochemistry and Molecular Biotechnology, University of Massachusetts Medical School, Worcester, MA 01605, USA

[b]Center for Systems Biology, Massachusetts General Hospital and Harvard Medical School, Boston, MA 02110, USA

[c]Department of Neurology, Lewis Katz School of Medicine at Temple University, Philadelphia, PA 19140, USA

[d]Department of Neurology, RNA Therapeutic Institute, Neuroscience Program, University of Massachusetts Medical School, Worcester, MA, USA

[e]Program in Chemical Biology, University of Massachusetts Medical School, Worcester, MA 01605, USA

Abstract

Alteration in protein citrullination (PC), a common posttranslational modification (PTM), contributes to pathogenesis in various inflammatory disorders. We previously reported that PC and protein arginine deiminase 2 (PAD2), the predominant enzyme isoform that catalyzes this PTM in the central nervous system (CNS), are altered in mouse models of amyotrophic lateral sclerosis (ALS). We now demonstrate that PAD2 expression and PC are altered in human postmortem ALS spinal cord and motor cortex compared to controls, increasing in astrocytes while trending lower

*Corresponding author at: Department of Biochemistry and Molecular Biotechnology, University of Massachusetts Medical School, 364 Plantation St, Worcester, MA 01605, USA. zuoshang.xu@umassmed.edu (Z. Xu).

Author contributions

Conceptualization: IOY, PRT, ZX; Investigation, data curation and analysis: IOY, ZX; Methodology: IOY, LWO, ZX; Project administration: IOY, ZX; Resources: IOY, SP, LWO, RHB, ZX; Supervision: ZX and PRT; Writing – original draft: IOY, ZX; Writing – review and editing: IOY, LWO, PRT, ZX; Funding acquisition: ZX and PRT.

Supplementary data to this article can be found online at https://doi.org/10.1016/j.nbd.2024.106414.

CRediT authorship contribution statement

Issa O. Yusuf: Writing – review & editing, Writing – original draft, Visualization, Validation, Resources, Project administration, Methodology, Investigation, Formal analysis, Data curation, Conceptualization. **Sepideh Parsi:** Resources, Investigation. **Lyle W. Ostrow:** Writing – review & editing, Resources, Methodology. **Robert H. Brown:** Resources. **Paul R. Thompson:** Writing – review & editing, Supervision, Funding acquisition, Conceptualization. **Zuoshang Xu:** Writing – review & editing, Writing – original draft, Supervision, Resources, Project administration, Methodology, Investigation, Funding acquisition, Formal analysis, Data curation, Conceptualization.

Declaration of competing interest

PRT holds equity in Padlock Therapeutics a subsidiary of Bristol Myers Squibb. The other authors have no competing interests to declare that are relevant to this article.

in neurons. Furthermore, PC is enriched in protein aggregates that contain the myelin proteins PLP and MBP in ALS. These results confirm our findings in ALS mouse models and suggest that altered PAD2 and PC contribute to neurodegeneration in ALS.

Keywords

Neurodegeneration; Deimination; Neurodegenerative disease; Myelin degeneration; Protein aggregation; Neuroinflammation

1. Introduction

Amyotrophic lateral sclerosis (ALS) is a fatal and progressive neurodegenerative disease that causes motor neuron degeneration, motor dysfunction, paralysis, and eventual death. ALS is categorized into sporadic cases (~90%) and familial cases (~10%). Mutations in many genes cause or enhance the risk of ALS. Multiple mechanisms are implicated in ALS pathogenesis, including protein aggregation, mitochondrial dysfunction, cytoskeletal disruption, neuroinflammation, abnormal RNA processing, oxidative stress, non-cell autonomous toxicity, and white matter degeneration, suggesting that aberrations in diverse pathways contribute to motor neuron degeneration. To date, the disease has no cure. Treatments capable of halting or reversing the disease progression remain to be developed (Akcimen et al., 2023; Mead et al., 2023; Younger and Brown Jr., 2023). Hence, continuous effort is required to push the frontiers of our understanding of the disease.

Protein arginine deiminase 2 (PAD2) belongs to a family of cysteine hydrolases known as PADs (Fuhrmann et al., 2015). PADs are differentially expressed in tissues, with PAD2 showing the highest expression level in the central nervous system (CNS) (Mondal and Thompson, 2019; Shimada et al., 2010). The activity of PADs is tightly regulated by calcium levels (Fujisaki and Sugawara, 1981). Under normal intracellular calcium concentrations (~100 nM), PADs are inactive. They are activated at high calcium levels (1–10 mM). Once activated, PADs catalyze a reaction known as protein citrullination (PC) or deimination, an irreversible posttranslational modification (PTM) that converts peptidylarginine to peptidyl-citrulline (Mondal and Thompson, 2019). The reaction results in a loss of positive charges, thereby impacting the ionic and hydrogen bond-forming abilities of proteins. These changes can alter protein structure, activities and interactions with other proteins and nucleic acids (Fuhrmann et al., 2015; Tilvawala et al., 2018). PADs citrullinate numerous protein substrates, thereby regulating cell signaling, immune responses, and gene expression (Tilvawala and Thompson, 2019).

PADs and PC are implicated in diverse pathologies, including COVID-19, atherosclerosis, rheumatoid arthritis, lupus, and cancers (Ciesielski et al., 2022; De Rycke et al., 2005; Song and Yu, 2019). Abnormal PAD2 activity and PC are also observed in neurodegenerative conditions, including Alzheimer's disease (AD), Parkinson's disease (PD), prion disease, Multiple sclerosis (MS), and ischemic and traumatic brain injuries (Jang et al., 2010; Jang et al., 2008; Lange et al., 2014; Lazarus et al., 2015; Mastronardi et al., 2006; Moscarello et al., 2002; Nicholas, 2011). In our previous studies, we provided evidence of PAD2 dysregulation and abnormal PC in ALS mouse models (Yusuf et al., 2022).

In the current study, we investigated changes in PAD2 and PC in sporadic ALS (sALS) postmortem CNS tissue samples. We show similar changes to what we observed in the mouse models. At the cellular level, PAD2 and PC accumulated prominently in astrocytes in the spinal cord and the motor cortex of ALS decedents. Strikingly, PC accumulated as protein aggregates that colocalized with myelin proteins proteolipid protein (PLP) and myelin basic protein (MBP) in the white matter of ALS spinal cord and cerebral sub-cortical motor pathways. These results show that increased PAD2 and aberrant PC are hallmarks of ALS pathology and support the hypothesis that dysregulation of PAD2 and PC contribute to ALS pathogenesis.

2. Material and methods

2.1. Human CNS tissue samples

Decedent demographics are summarized in Tables S1 and S2. Fresh frozen spinal cord tissues were processed for filter trap assay and Western blotting as described below. Spinal cord and motor cortex sections fixed in 10% formalin and paraffin-embedded were stained by immunohistochemistry (IHC) and immunofluorescence (IF) as detailed below.

2.2. Western blotting

Frozen tissues were homogenized in homogenization buffer [25 mM phosphate pH 7.6, 5 mM EDTA, 0.5% Triton X-100, 1% SDS, 0.5% deoxycholic acid, protease and phosphatase inhibitor cocktail; ThermoScientific™, 78,442] and then centrifuged at 16,060 x*g* for 10 min at 4 °C. The supernatant was collected as protein samples. Protein concentration was measured using Bradford assay (Bio-Rad 5,000,006). The samples were heated in Laemmli buffer (Bio-Rad 1,610,747) containing 10% β-Mercaptoethanol (Bio-Rad 1,610,710) at 95 °C for 10 min, and equal amounts of protein were loaded and subjected to sodium dodecyl sulfate polyacrylamide gel electrophoresis (SDS-PAGE) (Bio-Rad). Proteins on the gel were transferred to nitrocellulose membranes (Amersham™ Protran®, GE10600002). Blots were blocked with 5% (wt/vol) nonfat dry milk (Boston Bioproducts Inc., P-1400) in PBS for 1 h, followed by incubation with primary antibodies (Table S3) overnight at 4 °C. The blots were washed with phosphate-buffered saline with 0.1% Tween 20 (PBST) three times for 5 min each and then incubated with horseradish peroxidase (HRP)–conjugated secondary antibodies (Table S4) in PBST with 5% (wt/vol) nonfat dry milk for 1 h at room temperature (RT). Membranes were washed three times for 5 min each, and proteins were visualized using SuperSignal™ West Pico PLUS Chemiluminescent Substrate (Thermo Scientific™, 34,580) reagent and detected by the Amersham Imager 600 (GE). ImageJ software was used to quantify the integrated density of the protein bands.

2.3. Immunofluorescence and immunohistochemistry

For immunofluorescence staining of human samples, paraffin-embedded tissue sections were deparaffinized and hydrated by passing them through the following washes for 5 min each: Xylene, 2×; 100% ethanol, 2×; 95% ethanol, 1×; 70% ethanol, 1×; 50% ethanol, 1×; and tap water, 3×. Antigen retrieval was conducted by immersing slides in sodium citrate solution in a 60 °C covered water bath for 4 h. The sections were cooled down to RT and washed with tap water and 1× PBS, treated with BLOXALL® Endogenous blocking solution

(Vector Lab, SP-6000-100) for 10 min, washed with PBS for 10 min, permeabilized with 0.4% Triton-X100 in 1× PBS for 10 min, and washed gently with PBS three times for 5 min each. The sections were then incubated in blocking solution [5% donkey or goat serum (Sigma, D9663; Sigma, G9023), 0.15% Triton -X100, and (2%) nonfat dry milk in PBS, pH 7.4] for 1 h at RT, and then incubated with a primary antibody (Table S3) in the blocking solution for ~48 h at 4 °C. The sections were washed with PBS three times for 10 min each, then incubated with a secondary antibody (Table S4) in blocking buffer for 2 h at RT. The sections were washed with PBS three times for 10 min each. Finally, the sections were treated with TrueBlack® Lipofuscin Autofluorescence Quencher (Biotium, 23,007) for 15 s according to manufactural protocol, washed with PBS, and mounted using SouthernBiotech mounting medium containing DAPI (SouthernBiotech, 0100-20) and sealed with nail polish. Images of the spinal cord and motor cortex sections were taken with a confocal microscope (Leica) and analyzed as described below.

For immunohistochemistry, following deparaffinization, antigen retrieval and blocking and primary antibody (Table S3) incubation as described above for immunofluorescence, sections were washed with PBS three times for 10 min each, incubated with secondary biotinylated antibody (Table S4) in blocking buffer for 2 h at RT, washed with PBS three times for 10 min each, and then stained using Vectastain ABC kit, Elite PK-6100 standard, ImmPact DAB peroxidase Substrate kit (Vector Lab, SK-4105) following the manufacturer's instructions, and counterstained with Hematoxylene (Vector lab, H-3401). The sections were dehydrated by moving slides through the following solutions for 2 min each: 50%, 70%, 95%, 100% ethanol, and twice in Xylene. The slides were sealed with a Permount mounting medium (Fisher Chemical SP15-100). Images of the spinal cord sections were taken with a Nikon Optiphot microscope equipped with a SPOT Insight 2.0 Mp Firewire Color digital camera.

2.4. Quantitative image analysis

In each study, the staining and imaging parameters were set identically for all images taken. ImageJ was used to process and assess all images. Quantitative comparisons were carried out on sections processed at the same time. For quantification in neurons of the anterior horn spinal cord and motor cortex layer V, PAD2 or citrulline staining intensity was measured from the cell body of individual NF-H or NeuN-positive cells. Twelve to thirty cells in anterior horn of spinal cord and 35–60 cells in motor cortex were measured from each decedent and averaged to represent the measured value from an individual. For quantification of GFAP, total PAD2, and PC levels, the staining intensity was measured from 4 to 6 image frames (0.15 mm^2) in each decedent and were averaged. The values from the individuals in ALS and control groups were further averaged and compared statistically. The number of individuals in ALS and control groups are stated in the figure legends. Manders colocalization coefficient (MCC) for GFAP and PAD2 and for GFAP and PC was determined from the image frames by Just Another Colocalization Plugin (JACoP) (Bolte and Cordelieres, 2006; Dunn et al., 2011) as described in our previous report (Yusuf et al., 2022).

For quantification of aggregates, confocal images were taken from the spinal cord and subcortical white matter. Because the aggregates have high staining intensity, images were taken at relatively low exposure to eliminate background and low-intensity signals. A cut-off for aggregate size was set at 10 μm^2. Citrullination signals from other cellular processes, such as astrocytes, were excluded by applying a shape factor filter to include only structures with a shape circularity of 0.4–1. Few remaining linear astrocytic processes were eliminated manually. After the adjustments, the number of aggregates was measured from the area of interest. The numbers from 4 to 6 image frames (0.15 mm^2) in each decedent were averaged and the average was used to represent the number of aggregates in each decedent. The number of aggregates were normalized to the area of 1 mm^2. The normalized numbers from multiple decedents in ALS and control groups were further averaged and compared. For quantification of aggregate colocalization with myelin proteins, the MCC was determined by JACoP.

2.5. Protein citrulline modification

Protein citrulline was modified using the anti-modified citrulline detection kit (Millipore, 17-347B). Briefly, 5 mL of reagent A (2.5 mL of 0.5% $FeCl_3$ (Catalog #20-255) with 25 mL of water; 12.5 mL of 98% H_2SO_4 and 10 mL of 85% H_3PO_4) was mixed with 5 mL of reagent B (included in the kit) to make the modification buffer. For immunoblotting to detect citrullinated proteins, proteins were resolved by SDS-PAGE and transferred to the PVDF membrane (Thermo Scientific™, 88,518). The membranes were washed two times with tap water and incubated with the modification buffer. Blots were placed in a lightproof, air-tight container and incubated at 37 °C overnight without agitation. The modified blot was rinsed 4–5 times with tap water, blocked in freshly prepared 5% nonfat dry milk in tris-buffered saline with 0.1% Tween 20 (TBST) for 1 h at RT with constant agitation. Blots were incubated with 1:1000 dilution of anti-modified Citrulline antibody (Millipore, MABS487) diluted in freshly prepared TBST-Milk for 2 h at RT, washed three times with TBST for 10 min each, incubated with 1:2000 dilution of goat anti-Human IgG HRP-Conjugate in TBST-Milk for 1 h at RT, and washed three times with TBST for 10 min each. The blots were rinsed one time with water, and then SuperSignal™ West Pico PLUS Chemiluminescent Substrate was added to detect the signal.

For immunostaining to detect citrullinated proteins, the method of Asaga and Senshu was modified (Asaga and Senshu, 1993). The tissue sections were treated with the modification buffer described above and incubated at 37 °C overnight. The sections were washed with PBST three times for 10 min each, blocked for 1 h, and then incubated with primary antibody (anti-modified citrulline antibody, Millipore, MABS487, 1:100) overnight RT. The sections were washed with PBST three times for 10 min each and incubated with a secondary antibody (Table S4) for 2 h at RT. The steps following the secondary antibody incubation are described in the immunofluorescence and immunohistochemistry section.

2.6. Filter trap assay

Human lumbar spinal cords were homogenized using a handheld polytron for 20 s in lysis buffer [50 mM Tris-HCl, 150 mM NaCl, 0.5% deoxycholic acid, 1% (*v*/v) Triton X-100, 5 mM EDTA] with protease and phosphatase inhibitor cocktail (1:100 dilution, Thermo

Scientific™, 78,442). The tissue-to-buffer ratio was 1:10 (mg/μL). The homogenates were assayed for their protein concentration (Bradford assay). Two hundred micrograms (μg) of protein samples were equalized with lysis buffer to the same volume and diluted with 20 volumes of PBS (pH 7.4) containing 1% (vol/vol) SDS. The solution was sonicated (70 W, 50% output, 30 s) and then filtered under vacuum through a pre-wet 0.45 mm pore size PVDF membranes (Thermo Scientific™, 88,518) using a 96-well dot-blot apparatus (Schleicher and Schuell, Inc.). Each well was washed two times with PBS. The membrane was removed from the apparatus and rinsed in tap water. The following steps to detect citrullinated proteins and other protein aggregates are described in western blotting.

2.7. Statistical analyses

Results are shown as mean ± standard error of the mean (SEM). GraphPad Prism (GraphPad Software Inc. Version 8.4.3) was used to analyze statistical differences. The student's *t*-test was used to compare control and ALS. Statistical significance was set at $p < 0.05$.

3. Results

3.1. PAD2 expression is altered in astrocytes in ALS decedents

PAD2 expression was evaluated by Western blot of postmortem spinal cord protein homogenates. PAD2 expression was higher in ALS tissues than the non-ALS controls (Fig. 1). Next, cellular distribution was evaluated by immunohistochemistry (IHC) on spinal cord tissue sections. The results consistently demonstrated higher PAD2 staining in the anterior horn in ALS than in controls (Fig. 2A, B). The most intensely stained cells showed a morphology consistent with astrocytes (Fig. 2B, arrows), whereas neurons remained pale similar to the controls (Fig. 2B, open arrowheads). This observation was confirmed by double immunofluorescence (IF) microscopy. The intense PAD2 staining mainly colocalized with the reactive astrocyte marker GFAP and was increased in ALS (Fig. 2C, E, F), whereas low PAD2 staining colocalized with neuronal NF-H staining and was slightly lower in ALS than the controls (Fig. 2D, G).

Similarly, PAD2 staining was increased in astrocytes in the motor cortex in ALS compared to controls (Fig. 2H, I, arrows), whereas staining in neurons appeared weaker (Fig. 2I, open arrowheads). Double IF microscopy confirmed that the intense PAD2 staining colocalized with GFAP as in the spinal cord (Fig. 2J, S1), whereas PAD2 staining of cortical NeuN-positive neurons appeared similar in ALS and the controls (Fig. 2K, S2). The overall PAD2 staining and its colocalization with astrocytes were increased in ALS motor cortex compared to the controls, but these changes did not reach statistical significance (Fig. 2L, M). Quantification of PAD2 staining in neurons also showed no difference between ALS and the controls (Fig. 2N).

Next, we examined PAD2 expression in white matter (Fig. 3A, H). In the spinal cord, PAD2 IHC showed increased staining in glial cells in the corticospinal tract of both control and ALS cases (Fig. 3B, arrows). Overall PAD2 staining was increased in ALS compared with the controls (Fig. 3B). The GFAP and PAD2 signals mostly colocalized in ALS, but slightly

less so in the controls (Fig. 3C, D, E). Quantification of staining intensities showed that PAD2 was increased in ALS, whereas GFAP was not (Fig. 3F, G).

Similar patterns were found in the subcortical white matter of the motor cortex (Fig. 3H). IHC staining for PAD2 showed cells with astrocytic morphology in both ALS and controls (Fig. 3I, arrows). Double IF staining for GFAP and PAD2 confirmed the colocalization of PAD2 and GFAP signals (Fig. 3J, K, L). Both PAD2 and GFAP average staining intensity were increased to nearly double that seen in the controls. However, the differences did not reach statistical significance, probably due to the high variations among the samples (Fig. 3M, N).

We further investigated PAD2 expression in other cell types. By double IF staining for PAD2 and Olig2, we did not notice a significant change in PAD2 staining in oligodendrocytes in ALS (Fig. S3). Similarly, double IF staining for PAD2 and Iba1 did not show a significant difference of PAD2 expression in microglia (Figs. S4).

3.2. Protein citrullination is increased in astrocytes in ALS

Given the changes in PAD2 expression, we next investigated whether PC was altered. The levels of PC were measured using the anti-modified citrulline (AMC) method for Western blot (see Methods). ALS lumbar spinal cord showed higher levels of citrullinated proteins than the controls (Fig. 4). To determine the cell types where PC was increased, we adapted the AMC method to stain CNS tissue sections (see Methods). By AMC-IHC, the overall staining for PC was more intense in ALS than in controls in the anterior horn. In controls, large motor neuron cell bodies (Fig. 5A, open arrowheads) and astrocytes (Fig. 5A, arrows) were intensely stained. By contrast, few large motor neurons were observed in ALS, and these neurons appeared less intensely stained compared to the controls (Fig. 5A, open arrowheads). However, the staining for astrocytes (Fig. 5A, arrows) was stronger in ALS than in the controls.

To confirm the above observations, we performed double IF staining for GFAP and PC. Compared with controls, staining for PC increased significantly in ALS spinal cord anterior horn, and the staining signal was colocalized with GFAP (Fig. 5B, D, E). To determine neuronal PC levels, we performed double IF staining for NF-H and PC in the spinal cord anterior horn. Quantification of the PC staining intensity in the NF-H-positive cells showed a ~ 40% decrease in ALS compared to controls, although the decrease did not reach statistical significance (Fig. 5C, F).

Next, we examined the motor cortex and found similar changes as in the spinal cord. IHC staining revealed that, in controls, neurons (Fig. 5G, open arrowheads) and astrocytes (Fig. 5G, arrows) were strongly stained for citrullinated proteins. In ALS, neurons were stained with similar intensity as controls. However, the morphology of the neurons was less well defined, as manifested by poorly discernable nuclear boundaries (Fig. 5G, open arrowheads). The stained astrocytes were more numerous, but the staining intensity was similar to controls (Fig. 5G, arrows). To confirm this, we performed double IF staining. We found that the staining intensity for PC was significantly higher in ALS than in controls (Fig. 5H, J, S5), and the PC and GFAP colocalization was slightly higher in ALS than in controls,

but this difference did not reach statistical significance (Fig. 5H, K). PC staining levels in NeuN-positive cells were similar between the control and ALS (Fig. 5I, L, S6).

To confirm that PAD2 and PC are both increased in astrocytes in ALS, we performed double IF staining. In the gray matter of the spinal cord (Fig. 6A) and motor cortex (Fig. 6C), PAD2 and PC signals overlapped nearly completely in both controls and ALS. However, in the white matter, the staining showed a different pattern. Although PAD2 and PC signals mostly overlapped in controls, some intensely citrulline-positive structures did not overlap with PAD2 in ALS (Fig. 6B, D, arrowheads). These structures are protein aggregates that will be defined in the sections below.

We further examined other cell types. By double IF staining, we found that oligodendrocytes were weakly stained for citrullinated proteins but did not observe changes in ALS (Fig. S7). Similarly, we did not detect changes in PC levels in microglia (Fig. S8). These results show that PC is increased in astrocytes but not in other cell types in ALS motor cortices.

3.3. Citrullination marks protein aggregates in the white matter in ALS

We have previously shown that citrullination marks protein aggregates in white matter in two mouse models of ALS (Yusuf et al., 2022). IHC on human postmortem tissues similarly showed that PC was increased in both spinal cord and subcortical white matter of the motor cortex in ALS compared to controls (Fig. 7A, I). The most intense staining was in astrocytes (Fig. 7A, I, arrows) and in small amorphous foci suggestive of protein aggregates (Fig. 7A, I, arrowheads). To confirm these observations, we performed double IF staining for GFAP and PC. We found that PC colocalized with GFAP in both control and ALS (Fig. 7B, C, J, K), and this colocalization was strengthened in ALS, although this strengthening was significant only in the spinal cord (Fig. 7D, L). PC, but not GFAP, was significantly increased in ALS compared with the control (Fig. 7E, F, M, N). In addition, similar to the IHC staining (Fig. 7A, I), we observed amorphous foci that intensely stained for PC but not for GFAP (Fig. 7B, C, J, K, arrowheads), suggesting that these are protein aggregates and are not associated with astrocytes. We quantified the numbers of these foci and found that they were significantly higher in ALS than in the controls in the white matter (Fig. 7G, H, O). Interestingly, in the spinal cord, these foci also were on the spinothalamic tract (Fig. 7G, H), suggesting that citrullinated protein aggregates occur in both motor and sensory axon tracts.

3.4. Citrullinated protein aggregates are colocalized with myelin proteins in the CNS white matter in ALS decedents

We previously reported that the myelin proteins PLP and MBP colocalized with citrullinated protein aggregates in spinal cord white matter in ALS mouse models (Yusuf et al., 2022). To determine whether this is the case in human ALS, we performed double IF staining for PC and either PLP or MBP on spinal cord sections. PLP and MBP staining showed mostly ringlike patterns typical of normal myelin structure in control spinal cord cross-sections (Fig. 8A, B, arrows). These ringlike structures partially overlapped with the PC signal. In ALS, most of the PLP- and MBP-stained ringlike structures remained, but numerous amorphous aggregates exhibiting intense PLP and MBP staining were also observed (Fig.

8A, B, arrowheads). These aggregates increased significantly in ALS compared with controls and were mostly colocalized with the PC staining (Fig. 8C–G).

We observed the same changes in subcortical white matter as in the spinal cord white matter. PLP and MBP aggregates increased significantly in number in ALS compared to controls, and the aggregates colocalized with the PC staining (Fig. 9). In addition, we observed similar types of aggregates in the motor cortex (gray matter) in ALS (Fig. S9, arrowheads).

To further confirm the presence of these protein aggregates, we conducted a filter trap assay (see methods). We detected higher levels of citrullinated proteins and myelin proteins in the trapped protein aggregates in ALS samples compared to controls (Fig. 10A–F).

4. Discussion

We investigated PAD2 expression and PC in postmortem tissues from sporadic ALS decedents compared to non-neurologic controls. Our results show that PAD2 and PC are altered in ALS, increased in reactive astrocytes, and trending lower in neurons in ALS spinal cords, while unchanged in motor cortex (Figs. 1–5). Furthermore, PC is enriched in insoluble protein aggregates (Fig. 10) and colocalizes with the myelin proteins PLP and MBP. The aggregates do not contain PAD2 and are not associated with astrocytes (Figs. 6–9). These observations confirm our findings in ALS mouse models (Yusuf et al., 2022).

Nevertheless, some differences are notable between our findings in the human sporadic ALS tissues compared with the ALS mouse models. For example, the increase of PAD2 and PC was less pronounced in human sporadic ALS than in the mice. Furthermore, the decrease of PAD2 and PC in neurons was modest and did not reach statistical significance in the human tissues. Strikingly, the large increases in GFAP levels in the ALS mouse models are not detected in human ALS (Figs. 3, 7). Overall, the degree of changes observed in human sALS is smaller than in the ALS mouse models (Yusuf et al., 2022). Several factors may contribute to the smaller differences in the human decedent tissues. Both control and ALS human samples were much more variable than the mouse samples. This is not unexpected, as the mouse tissues were collected from the models raised in a controlled environment and collected at well-defined disease stages, whereas the human disease develops in highly variable environments and ends in divergent conditions. Additionally, the mouse models were constructed based on two genetic subtypes of ALS-SOD1 and ALS-PFN1, and therefore, may better represent ALS with these specific mutations. By contrast, human sALS is known to be a considerably more variable disease. Furthermore, human postmortem ALS tissues often show highly variable pathologic involvement in different regions of the neuroaxis within each decedent. Despite this, the same qualitative changes were observed in the mouse and human tissues, suggesting that abnormalities of PAD2 and PC are found broadly across different types of ALS.

Increased PAD2 and PC in astrocytes has similarly been described in other human neurodegenerative diseases and their animal models. The changes overlap with GFAP, a pan-reactive astrocyte marker, in vulnerable areas of the diseases. In Alzheimer’s disease (AD), the hippocampus and frontal cortex show reactive astrocytes with high PAD2 and

PC, especially around extracellular plaques (Ishigami et al., 2005; Nicholas, 2013). In PD, surviving dopamine neurons in the substantia nigra are surrounded by reactive astrocytes immunoreactive for PC (Nicholas, 2011). In multiple sclerosis (MS), reactive astrocytes within demyelinating lesions show increased PC (Bradford et al., 2014). In sporadic Creutzfeldt-Jakob disease (sCJD), PAD2 and PC increased mainly in astrocytes in the frontal cortex (Jang et al., 2010). In this study, we observed increases of PC and PAD2 in astrocytes in ALS spinal cord and motor cortex, although the increases of PAD2 in the motor cortex did not reach statistical significance (Figs. 2, 3, 5, 7).

We did not find significant changes to neuronal PAD2 and PC in human ALS in this study, although decreased neuronal staining was observed in the spinal cord compared to controls (Figs. 2, 5). These observations differ from the decreases that we reported in mouse ALS models (Yusuf et al., 2022). Published reports in other neurodegenerative disorders show similarly variable results in neurons. For example, while some published studies showed elevated PC levels in surviving dopamine neurons in the substantia nigra in PD (Nicholas, 2011) and in cortical pyramidal and hippocampal neurons in AD (Acharya et al., 2012), other studies only found increased levels in astrocytes (Ishigami et al., 2005; Nicholas, 2013). Predominantly astrocytic increases were also reported in other neurodegenerative conditions such as prion disease and multiple sclerosis (Bradford et al., 2014; Jang et al., 2010).

Protein aggregates are hallmarks of many neurodegenerative disorders (Chiti and Dobson, 2017; Soto and Pritzkow, 2018). The aggregates are often enriched with post-translationally modified proteins, e.g., phosphorylated tau in AD and frontotemporal dementia (FTD), phosphorylated α-synuclein in PD and multiple system atrophy (MSA), and phosphorylated TDP-43 (pTDP-43) in ALS, FTD, AD, and Limbic-predominant age-related TDP-43 encephalopathy (LATE). The type and distribution of these aggregates have been instrumental in disease classification and staging (Aksman et al., 2023; Braak and Braak, 1995; Braak et al., 2003; Brettschneider et al., 2013; Iqbal et al., 2016; Josephs et al., 2016; Koga et al., 2021; Nelson et al., 2019; Scheres et al., 2023; Young et al., 2023). In this study, we demonstrated protein aggregates that contain abundant citrullinated proteins and myelin proteins PLP and MBP in ALS white matter (Figs. 6–10). Because the pTDP-43 staging data is not available for the ALS decedents used in this study, a correlation between the distribution of PC-positive aggregates and pTDP-43 is not feasible. Nevertheless, PAD2 and PC may represent a new class of protein aggregates that can be used to stage the progression of white matter degeneration in future studies.

How the aggregates with enriched PC and myelin proteins form and how they contribute to neurodegeneration remain to be determined. PLP and MBP are the two most abundant proteins in myelin and together constitute ~70% of total myelin proteins (Gargareta et al., 2022; Jahn et al., 2020). Whether PLP is citrullinated is not known. However, MBP citrullination is well documented and contributes to myelin maturation during development and autoimmunity against myelin in MS (Moscarello et al., 2007; Yang et al., 2016). MBP also is an intrinsically disordered protein, a characteristic shared with other aggregation-prone proteins (Harauz et al., 2004; Tsoi et al., 2023). In ALS, MBP citrullination

could cause its dissociation from the membrane, thereby enhancing the probability of its aggregation and facilitating myelin degeneration (Yusuf et al., 2022).

A key question from our findings is how PC impacts disease, i.e., whether it exacerbates or ameliorates the disease. Answering this question will require further investigation. Nevertheless, experiments on other disease models may offer clues. One study reported that PAD2 knockout did not affect the clinical phenotype in an experimental autoimmune encephalomyelitis (EAE) model, even though PC was reduced (Raijmakers et al., 2006). On the other hand, another study showed that overexpression of PAD2 is sufficient to cause demyelination and neuroinflammation (Musse et al., 2008). Additionally, PAD inhibitors have been shown to be therapeutically efficacious in many inflammatory disease models (Mondal and Thompson, 2019; Padhy et al., 2023). Neurodegenerative conditions often involve neuroinflammation (Ransohoff, 2016; Wilson 3rd et al., 2023). Indeed, PAD inhibitors have been demonstrated to protect against neurodegeneration in MS and CNS injury models (Lange et al., 2011; Lange et al., 2014; Moscarello et al., 2013). Neuroinflammation has been implicated in ALS disease progression (He et al., 2023; Rodrigues Lima-Junior et al., 2021). Similar to other inflammatory diseases, PC may contribute to neuroinflammation in ALS. Therefore, PAD inhibition could lessen neuroinflammation and be therapeutically beneficial.

In summary, we have shown that PAD2 and PC are upregulated in the spinal cord and motor cortex in postmortem tissues from sporadic ALS decedents. This upregulation is particularly pronounced in astrocytes. In the white matter, PC is highly enriched in protein aggregates that also contain abundant myelin proteins PLP and MBP. These results confirm our previous observation in ALS mouse models and suggest that this pathology may be universal in different types of ALS. Further studies will be needed to understand how PAD2 and PC upregulation impact astrogliosis, protein aggregation, myelin degeneration, and neuroinflammation. However, successes from studies to treat neurodegenerative conditions and other inflammatory conditions by inhibiting PC using PAD inhibitors suggest that inhibition of PC may be beneficial for the treatment of ALS and other neurodegenerative conditions.

Supplementary Material

Refer to Web version on PubMed Central for supplementary material.

Acknowledgments

The authors are grateful for the support from the core facilities at the University of Massachusetts Chan Medical School, including Morphology Core, Confocal Microscopy Core managed by Dr. Jeffrey Nickerson and Dr. Kerstin Nundel, and the Department of Animal Medicine. We would like to thank the Target ALS Postmortem Tissue Core, Johns Hopkins University, the University of California at San Diego, and Georgetown University for providing postmortem tissues and slides and the associated de-identified data, and Kathleen Wilsbach and Kathryn Gallo for coordinating the human decedent tissues and data.

Funding

This work was supported by grants from the Angel Fund for ALS Research, NIH/NINDS RO1-NS118145 to ZX and PRT, and NIH/NIGMS R35 GM118112 to PRT.

Data availability

All data supporting the conclusions of this article are included within the article and its supplementary materials.

References

Acharya NK, et al. , 2012. Neuronal PAD4 expression and protein citrullination: possible role in production of autoantibodies associated with neurodegenerative disease. J. Autoimmun 38, 369–380. [PubMed: 22560840]

Akcimen F, et al. , 2023. Amyotrophic lateral sclerosis: translating genetic discoveries into therapies. Nat. Rev. Genet 24, 642–658. [PubMed: 37024676]

Aksman LM, et al. , 2023. A data-driven study of Alzheimer's disease related amyloid and tau pathology progression. Brain

Asaga H, Senshu T, 1993. Combined biochemical and immunocytochemical analyses of postmortem protein deimination in the rat spinal cord. Cell Biol. Int 17, 525–532. [PubMed: 8339070]

Bolte S, Cordelieres FP, 2006. A guided tour into subcellular colocalization analysis in light microscopy. J. Microsc 224, 213–232. [PubMed: 17210054]

Braak H, Braak E, 1995. Staging of Alzheimer's disease-related neurofibrillary changes. Neurobiol. Aging 16, 271–278 discussion 278–84. [PubMed: 7566337]

Braak H, et al. , 2003. Staging of brain pathology related to sporadic Parkinson's disease. Neurobiol. Aging 24, 197–211. [PubMed: 12498954]

Bradford CM, et al. , 2014. Localisation of citrullinated proteins in normal appearing white matter and lesions in the central nervous system in multiple sclerosis. J. Neuroimmunol 273, 85–95. [PubMed: 24907905]

Brettschneider J, et al. , 2013. Stages of pTDP-43 pathology in amyotrophic lateral sclerosis. Ann. Neurol 74, 20–38. [PubMed: 23686809]

Chiti F, Dobson CM, 2017. Protein Misfolding, amyloid formation, and human disease: a summary of Progress over the last decade. Annu. Rev. Biochem 86, 27–68. [PubMed: 28498720]

Ciesielski O, et al. , 2022. Citrullination in the pathology of inflammatory and autoimmune disorders: recent advances and future perspectives. Cell. Mol. Life Sci 79, 94. [PubMed: 35079870]

De Rycke L, et al. , 2005. Synovial intracellular citrullinated proteins colocalizing with peptidyl arginine deiminase as pathophysiologically relevant antigenic determinants of rheumatoid arthritis-specific humoral autoimmunity. Arthritis Rheum 52, 2323–2330. [PubMed: 16052592]

Dunn KW, et al. , 2011. A practical guide to evaluating colocalization in biological microscopy. Am. J. Phys. Cell Phys 300, C723–C742.

Fuhrmann J, et al. , 2015. Chemical biology of protein arginine modifications in epigenetic regulation. Chem. Rev 115, 5413–5461. [PubMed: 25970731]

Fujisaki M, Sugawara K, 1981. Properties of peptidylarginine deiminase from the epidermis of newborn rats. J. Biochem 89, 257–263. [PubMed: 7217033]

Gargareta VI, et al. , 2022. Conservation and divergence of myelin proteome and oligodendrocyte transcriptome profiles between humans and mice. Elife 11.

Harauz G, et al. , 2004. Myelin basic protein-diverse conformational states of an intrinsically unstructured protein and its roles in myelin assembly and multiple sclerosis. Micron 35, 503–542. [PubMed: 15219899]

He D, et al. , 2023. The Inflammatory Puzzle: Piecing Together the Links between Neuroinflammation and Amyotrophic Lateral Sclerosis. Aging Dis

Iqbal K, et al. , 2016. Tau and neurodegenerative disease: the story so far. Nat. Rev. Neurol 12, 15–27. [PubMed: 26635213]

Ishigami A, et al. , 2005. Abnormal accumulation of citrullinated proteins catalyzed by peptidylarginine deiminase in hippocampal extracts from patients with Alzheimer's disease. J. Neurosci. Res 80, 120–128. [PubMed: 15704193]

Jahn O, et al. , 2020. The CNS myelin proteome: deep profile and persistence after postmortem delay. Front. Cell. Neurosci 14, 239. [PubMed: 32973451]

Jang B, et al. , 2008. Accumulation of citrullinated proteins by up-regulated peptidylarginine deiminase 2 in brains of scrapie-infected mice: a possible role in pathogenesis. Am. J. Pathol 173, 1129–1142. [PubMed: 18787103]

Jang B, et al. , 2010. Involvement of peptidylarginine deiminase-mediated post-translational citrullination in pathogenesis of sporadic Creutzfeldt-Jakob disease. Acta Neuropathol 119, 199–210. [PubMed: 20013286]

Josephs KA, et al. , 2016. Updated TDP-43 in Alzheimer's disease staging scheme. Acta Neuropathol 131, 571–585. [PubMed: 26810071]

Koga S, et al. , 2021. Neuropathology and molecular diagnosis of Synucleinopathies. Mol. Neurodegener 16, 83. [PubMed: 34922583]

Lange S, et al. , 2011. Protein deiminases: new players in the developmentally regulated loss of neural regenerative ability. Dev. Biol 355, 205–214. [PubMed: 21539830]

Lange S, et al. , 2014. Peptidylarginine deiminases: novel drug targets for prevention of neuronal damage following hypoxic ischemic insult (HI) in neonates. J. Neurochem 130, 555–562. [PubMed: 24762056]

Lazarus RC, et al. , 2015. Protein Citrullination: a proposed mechanism for pathology in traumatic brain injury. Front. Neurol 6, 204. [PubMed: 26441823]

Mastronardi FG, et al. , 2006. Increased citrullination of histone H3 in multiple sclerosis brain and animal models of demyelination: a role for tumor necrosis factor-induced peptidylarginine deiminase 4 translocation. J. Neurosci 26, 11387–11396. [PubMed: 17079667]

Mead RJ, et al. , 2023. Amyotrophic lateral sclerosis: a neurodegenerative disorder poised for successful therapeutic translation. Nat. Rev. Drug Discov 22, 185–212. [PubMed: 36543887]

Mondal S, Thompson PR, 2019. Protein arginine deiminases (PADs): biochemistry and chemical biology of protein Citrullination. Acc. Chem. Res 52, 818–832. [PubMed: 30844238]

Moscarello MA, et al. , 2002. Peptidylarginine deiminase: a candidate factor in demyelinating disease. J. Neurochem 81, 335–343. [PubMed: 12064481]

Moscarello MA, et al. , 2007. The role of citrullinated proteins suggests a novel mechanism in the pathogenesis of multiple sclerosis. Neurochem. Res 32, 251–256. [PubMed: 17031564]

Moscarello MA, et al. , 2013. Inhibition of peptidyl-arginine deiminases reverses protein-hypercitrullination and disease in mouse models of multiple sclerosis. Dis. Model. Mech 6, 467–478. [PubMed: 23118341]

Musse AA, et al. , 2008. Peptidylarginine deiminase 2 (PAD2) overexpression in transgenic mice leads to myelin loss in the central nervous system. Dis. Model. Mech 1, 229–240. [PubMed: 19093029]

Nelson PT, et al. , 2019. Limbic-predominant age-related TDP-43 encephalopathy (LATE): consensus working group report. Brain 142, 1503–1527. [PubMed: 31039256]

Nicholas AP, 2011. Dual immunofluorescence study of citrullinated proteins in Parkinson diseased substantia nigra. Neurosci. Lett 495, 26–29. [PubMed: 21414385]

Nicholas AP, 2013. Dual immunofluorescence study of citrullinated proteins in Alzheimer diseased frontal cortex. Neurosci. Lett 545, 107–111. [PubMed: 23648390]

Padhy DS, et al. , 2023. Selective inhibition of peptidyl-arginine deiminase (PAD): can it control multiple inflammatory disorders as a promising therapeutic strategy? Inflammopharmacology 31, 731–744. [PubMed: 36806957]

Raijmakers R, et al. , 2006. Experimental autoimmune encephalomyelitis induction in peptidylarginine deiminase 2 knockout mice. J. Comp. Neurol 498, 217–226. [PubMed: 16856138]

Ransohoff RM, 2016. How neuroinflammation contributes to neurodegeneration. Science 353, 777–783. [PubMed: 27540165]

Rodrigues Lima-Junior J, et al. , 2021. The role of immune-mediated alterations and disorders in ALS disease. Hum. Immunol 82, 155–161. [PubMed: 33583639]

Scheres SHW, et al. , 2023. Molecular pathology of neurodegenerative diseases by cryo-EM of amyloids. Nature 621, 701–710. [PubMed: 37758888]

Shimada N, et al. , 2010. Developmental and age-related changes of peptidylarginine deiminase 2 in the mouse brain. J. Neurosci. Res 88, 798–806. [PubMed: 19830834]

Song S, Yu Y, 2019. Progression on Citrullination of proteins in gastrointestinal cancers. Front. Oncol 9, 15. [PubMed: 30740359]

Soto C, Pritzkow S, 2018. Protein misfolding, aggregation, and conformational strains in neurodegenerative diseases. Nat. Neurosci 21, 1332–1340. [PubMed: 30250260]

Tilvawala R, Thompson PR, 2019. Peptidyl arginine deiminases: detection and functional analysis of protein citrullination. Curr. Opin. Struct. Biol 59, 205–215. [PubMed: 30833201]

Tilvawala R, et al. , 2018. The rheumatoid arthritis-associated Citrullinome. Cell Chem. Biol 25 (691–704), e6.

Tsoi PS, et al. , 2023. Aggregation of disordered proteins associated with neurodegeneration. Int. J. Mol. Sci 24. [PubMed: 38203194]

Wilson DM 3rd, et al. , 2023. Hallmarks of neurodegenerative diseases. Cell 186, 693–714. [PubMed: 36803602]

Yang L, et al. , 2016. Myelin basic protein Citrullination in multiple sclerosis: a potential therapeutic target for the pathology. Neurochem. Res 41, 1845–1856. [PubMed: 27097548]

Young AL, et al. , 2023. Data-driven neuropathological staging and subtyping of TDP-43 proteinopathies. Brain 146, 2975–2988. [PubMed: 37150879]

Younger DS, Brown RH Jr., 2023. Amyotrophic lateral sclerosis. Handb. Clin. Neurol 196, 203–229. [PubMed: 37620070]

Yusuf IO, et al. , 2022. Protein citrullination marks myelin protein aggregation and disease progression in mouse ALS models. Acta Neuropathol. Commun 10, 135. [PubMed: 36076282]

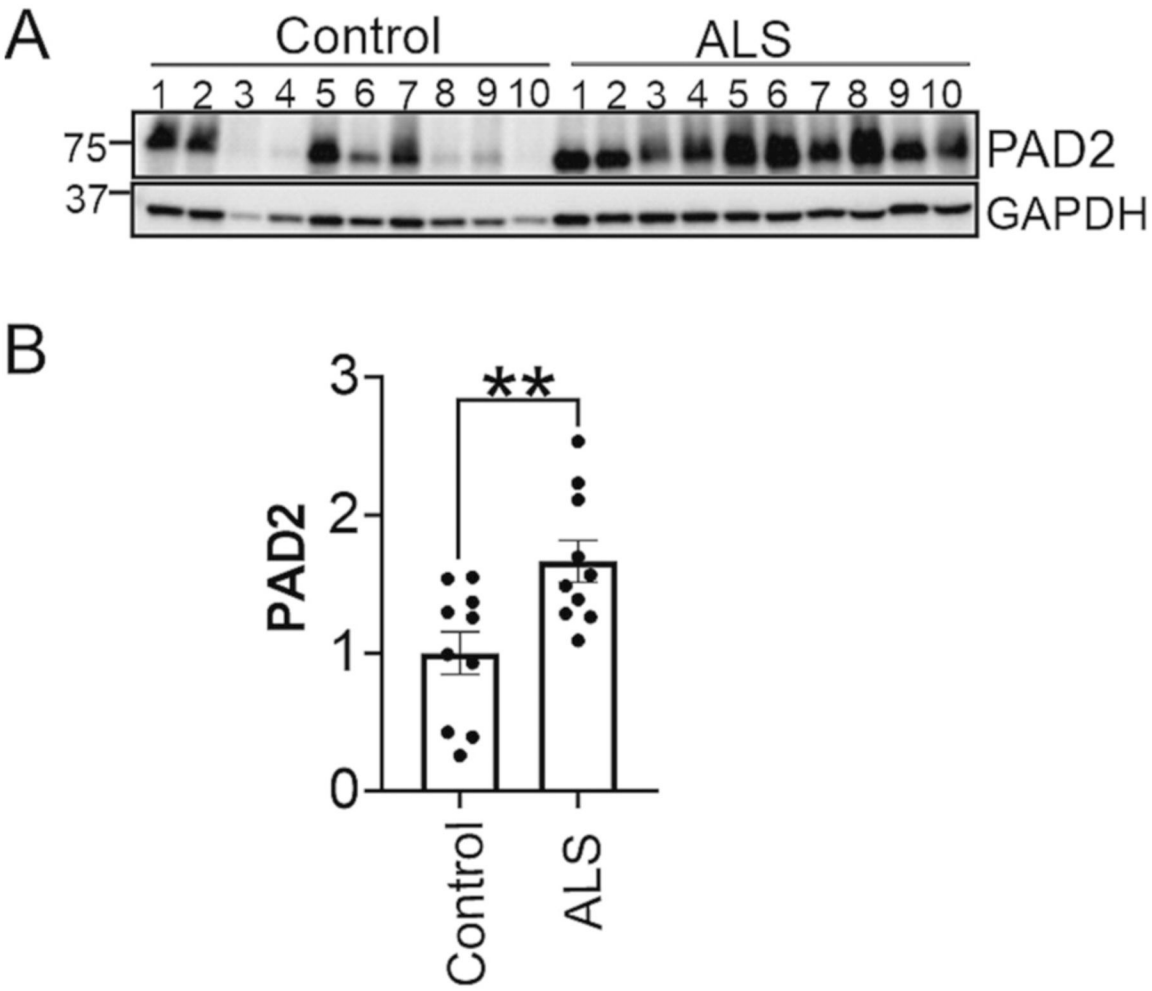

Fig. 1.

PAD2 expression is increased in the spinal cord of ALS decedents. (A) Western blot of PAD2 from the lumbar spinal cord of ALS decedents and non-ALS controls. (B) Quantification of PAD2 levels in the blot as illustrated in A. Depicted are ratios of PAD2 staining density over GAPDH staining density from each decedent and the averages of control and ALS groups ± standard error. Student *t*-test was used to compare ALS with controls; ** = $p < 0.01$; $n = 10$ per sample group.

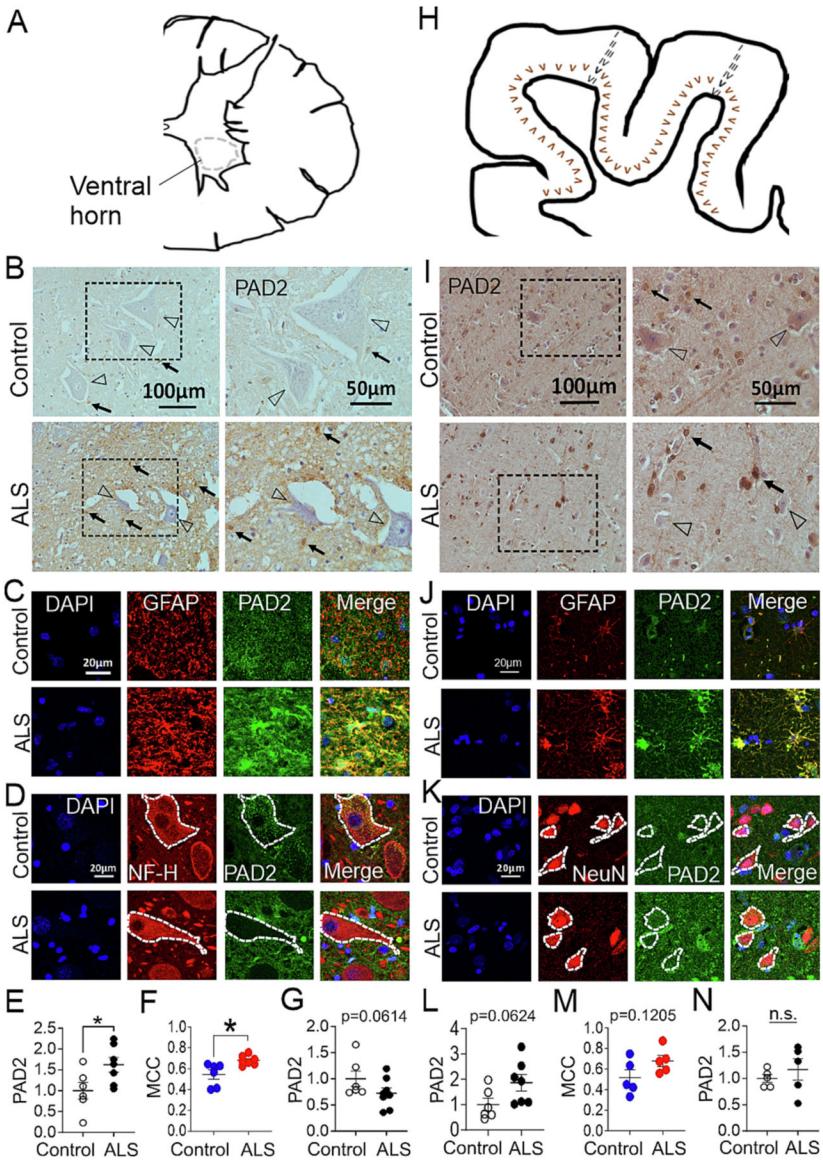

Fig. 2.

PAD2 is increased in astrocytes in the gray matter of spinal cords and motor cortices, slightly lower in spinal cord neurons, and unchanged in cortical neurons in ALS decedents. (A) A schematic illustration of the thoracic spinal cord showing the region of interest (gray dashed lines) that was imaged in B-D. (B) Immunohistochemistry (IHC) of PAD2 in spinal cord. The right panels are enlarged views of the boxed areas in the left panels. Open arrowheads point to motor neurons, and arrows point to astrocytes. (C, D) Double immunofluorescent (IF) staining for PAD2 with GFAP and NF-H, respectively. (E) Quantification of total PAD2 staining intensity from images as illustrated in C. (F) Mander's colocalization coefficient of GFAP and PAD2 in C. $n = 6$ in control and 7 in ALS groups in E and F. (G) Quantification of PAD2 staining in NF-H-positive cells from images as illustrated in D. n = 6 in control and 8 in ALS groups. (H) A schematic illustration of an area of the motor cortex showing the region of interest (layer v) that was imaged in I-K. (I) IHC

of PAD2 in the motor cortex layer V. The right panels are enlarged views of the boxed areas in the left panels. Open arrowheads point to neurons, and arrows point to possible astrocytes. (J, K) Double IF staining for PAD2 with GFAP and NeuN, respectively. (L) Quantification of total PAD2 staining intensity from images as illustrated in J. n = 6 in control and 7 in ALS groups. (M) Mander's colocalization coefficient of GFAP and PAD2 in J. (N) Quantification of PAD2 staining intensity in NeuN-positive cells from images as illustrated in K. $n = 5$ in each group in M and N. Shown in all quantitative graphs of staining intensity in this and subsequent figures are the measured values from individual decedents (circles), and the average in ALS and control groups ± standard error. Student *t*-test was used to compare ALS with controls; $*p < 0.05$.

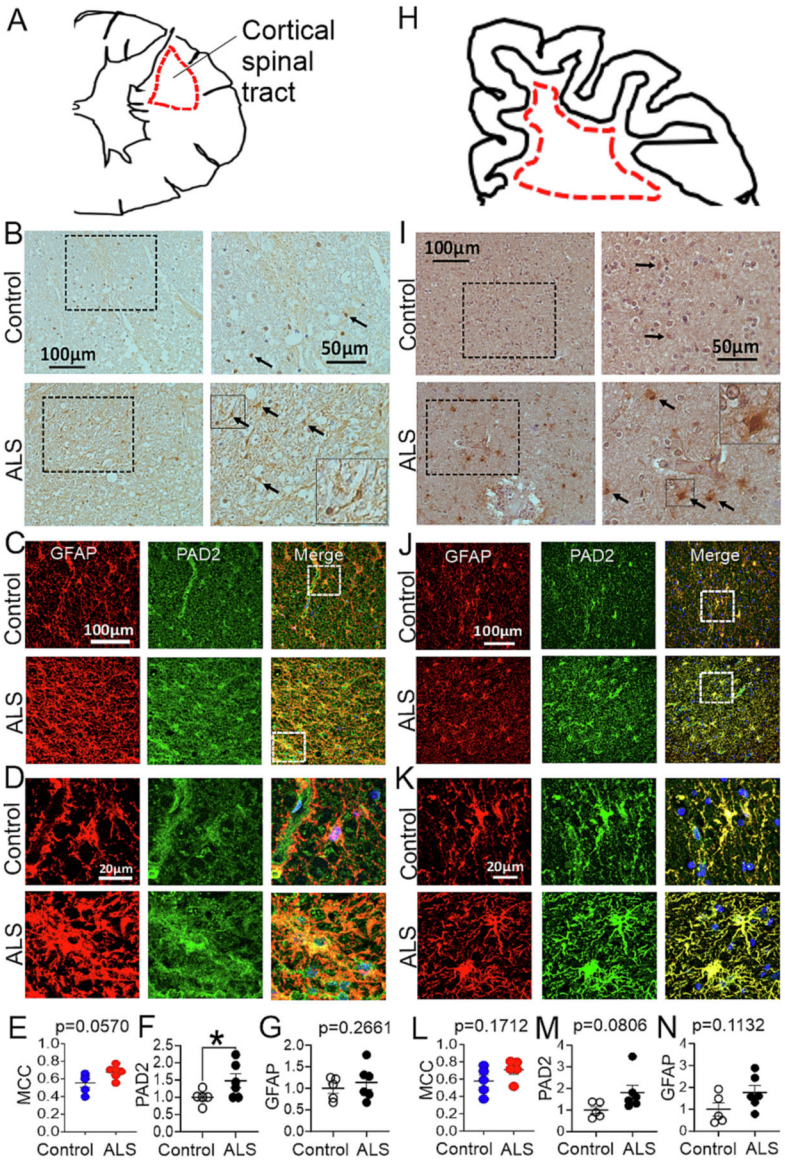

Fig. 3.

PAD2 is increased in astrocytes in the white matter of spinal cords and sub-motor cortices in ALS decedents. (A) A schematic illustration showing the region of interest, the corticospinal tract of the spinal cord (red dash lines) that were imaged in B-D. (B) IHC of PAD2 in spinal cords. The right panels are enlarged views of the boxed areas in the left panels. Arrows point to astrocytes. (C) Double IF staining for GFAP and PAD2 in spinal cords. (D) Enlarged views of the boxed area in C. (E) Mander's colocalization coefficient of GFAP and PAD2 from images as illustrated in C. (F, G) Quantification of staining intensity of PAD2 and GFAP, respectively, from images as illustrated in C. $n = 5$ in control and 6 in ALS groups in *E*-G. (H) A schematic illustration showing the region of interest, the subcortical white matter (red dash lines) that were imaged in I-K. (I) IHC of PAD2 in subcortical white matter. The right panels are enlarged views of the boxed areas in the left panels. Arrows point to astrocytes. (J) Double IF staining for GFAP and PAD2 in the subcortical white matter. (K)

Enlarged views of the boxed area in J. (L) Mander's colocalization coefficient of GFAP and PAD2 from images as illustrated in J. n = 5 in both groups. (M, N) Quantification of staining intensity of PAD2 and GFAP, respectively, from images as illustrated in J. n = 5 in control and 6 in ALS groups. Student *t*-test was used to compare ALS with controls, $*p < 0.05$.

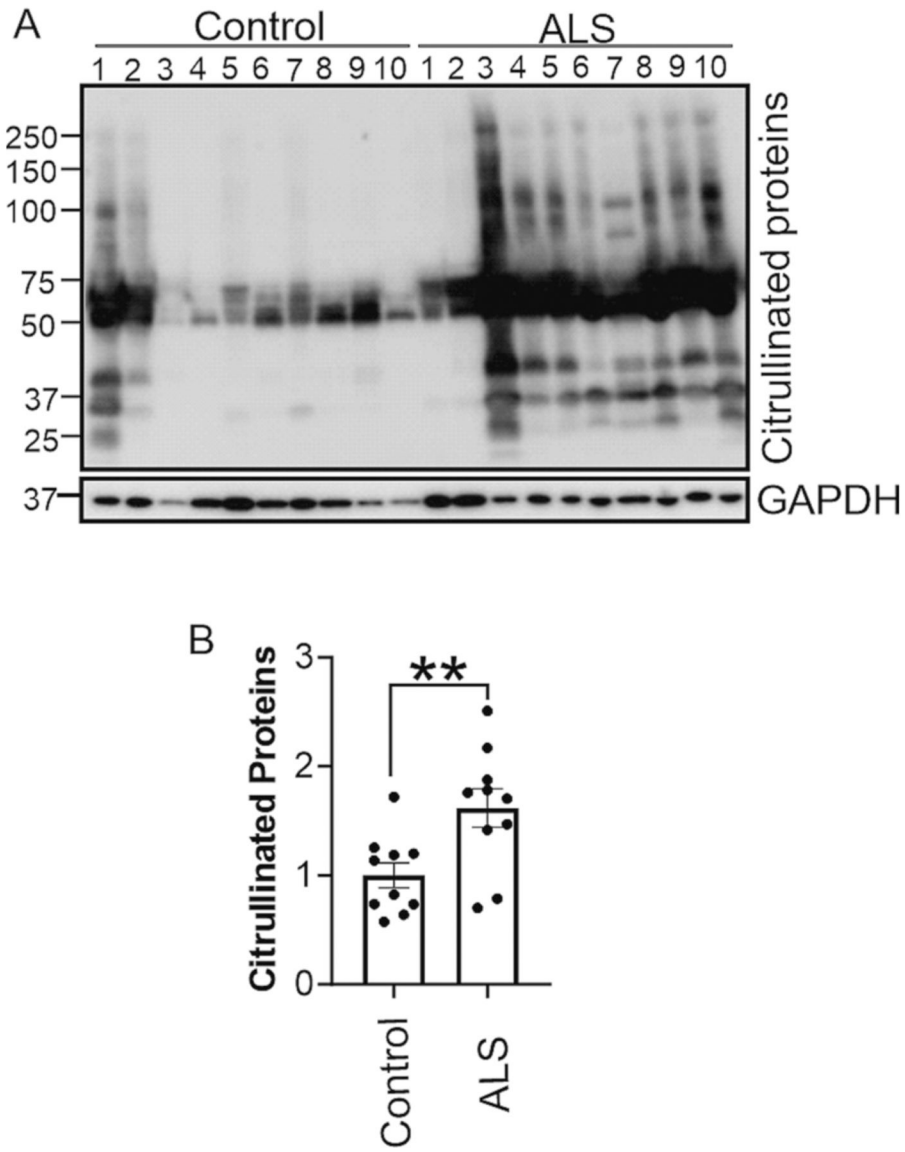

Fig. 4.

Protein citrullination (PC) is increased in the spinal cord of ALS decedents. (A) Western blot of citrullinated proteins from the lumbar spinal cord of ALS decedents and non-ALS controls. (B) Quantification of PC signal density in A. Depicted are ratios of PC staining density measured from each lane over GAPDH staining density from each decedent (circles) and the averages of control and ALS groups ± standard error. Student *t*-test was used to compare ALS with controls, ** = $p < 0.01$. $n = 10$ per sample group.

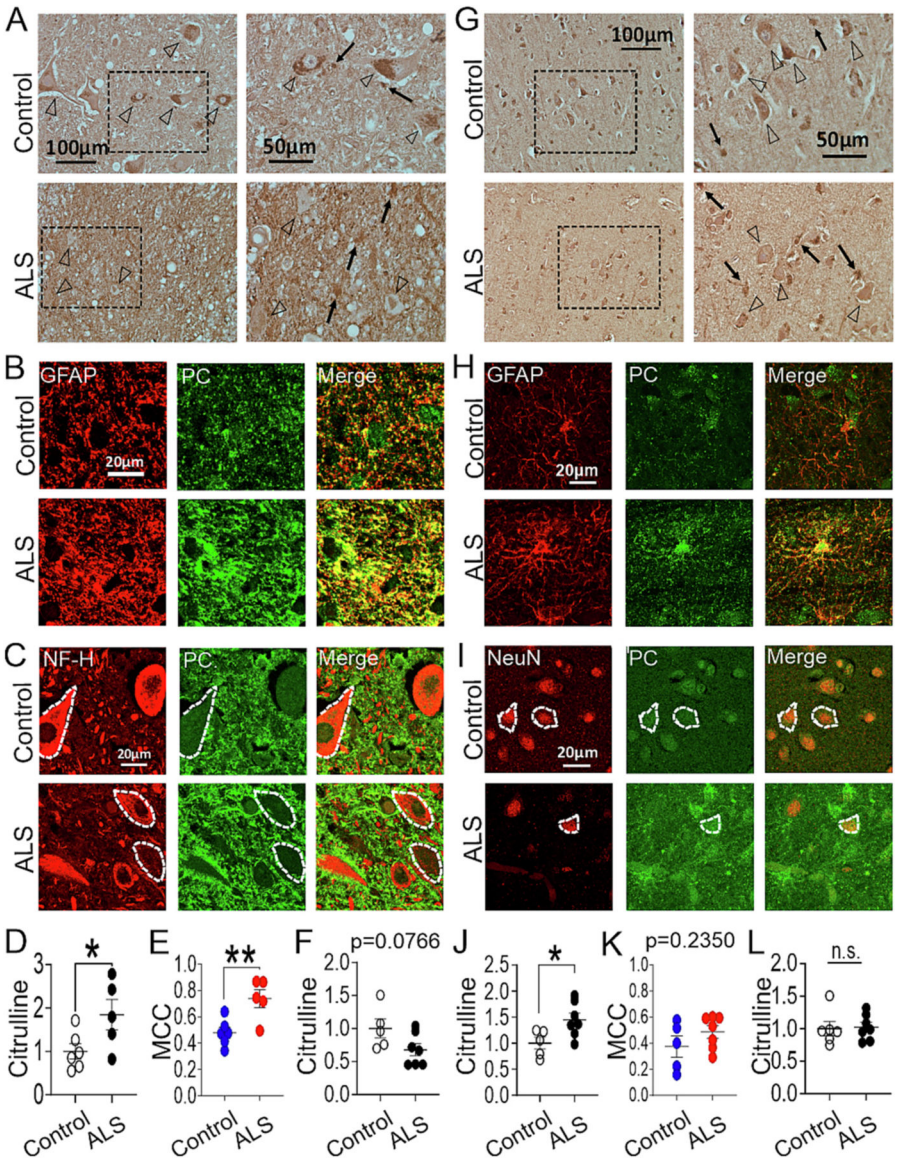

Fig. 5.

PC is increased in astrocytes in the spinal cord and the motor cortex but not significantly altered in neurons in ALS decedents. The sampling areas are the same as shown in Fig. 2A, H. (A) IHC of PC in the spinal cord. The right panels are enlarged views of the boxed areas in the left panels. Open arrowheads point to motor neurons, and arrows point to astrocytes. (B, C) Double IF staining for PC with GFAP and NF-H, respectively. (D) Quantification of total PC staining intensity from images as shown in B. n = 6 in control and 5 in ALS groups. (E) Mander's colocalization coefficient of GFAP and PC in B. n = 6 in control and 5 in ALS groups. (F) Quantification of PC staining intensity in NF-H-positive cells as shown in C. n = 5 in control and 7 in ALS groups. (G) IHC of PC in the motor cortex layer V. The right panels are enlarged views of the boxed areas in the left panels. Open arrowheads point to neurons, and arrows point to possible astrocytes. (H, I) Double IF staining for PC with GFAP and NeuN, respectively. (J) Quantification of total PC staining intensity from

images as shown in H. (K) Mander's colocalization coefficient of GFAP and PC in H. (L) Quantification of PC staining intensity in NeuN-positive cells as shown in I. n = 5 in control and 7 in ALS groups in J, K, and L. Student t-test was used to compare ALS with controls, *$p < 0.05$, **p < 0.01.

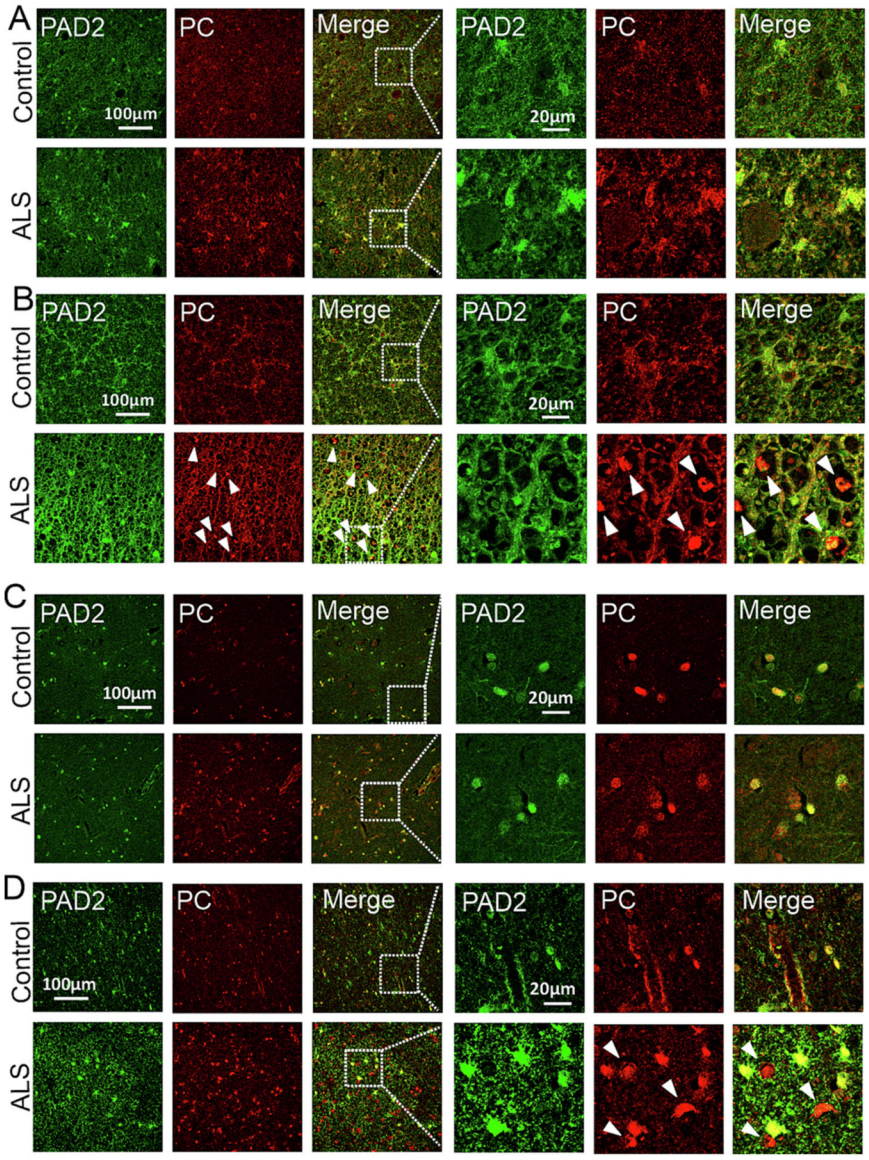

Fig. 6.

PAD2 and PC are both increased and colocalized in astrocytes in the spinal cord and motor cortex. (A, B) Double IF staining for PAD2 and PC in spinal cord anterior horn and white matter, respectively. (C, D) Double IF staining for PAD2 and PC in motor cortex and subcortical white matter, respectively. Arrowheads point to PC-positive aggregates that are independent of astrocytes (see text).

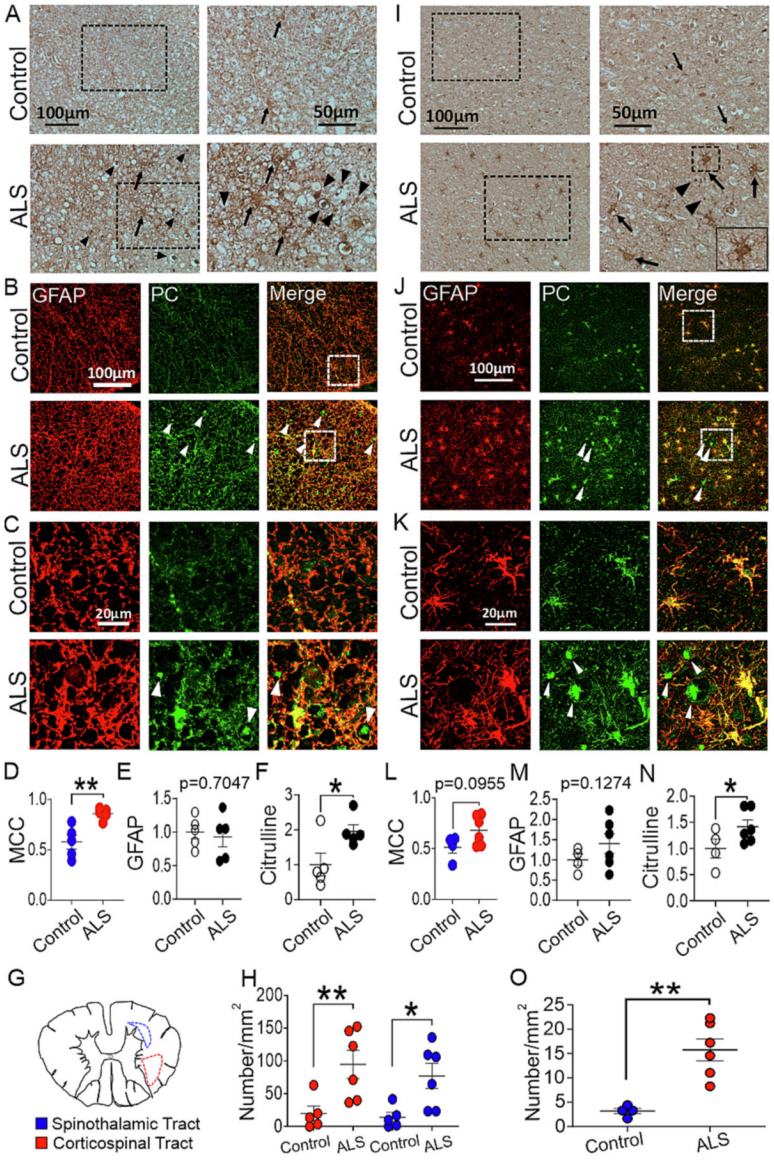

Fig. 7.

PC is accumulated in astrocytes and protein aggregates in the white matter of the spinal cord and motor cortex in ALS decedents. The sampling areas are the same as shown in Fig. 3A, H unless indicated otherwise. (A) IHC of PC in spinal cord white matter. The right panels are enlarged views of the boxed areas in the left panels. Arrows point to astrocytes, and arrowheads point to aggregate-like structures. (B) Double IF staining for GFAP and PC in spinal cord white matter. (C) Enlarged views of the boxed area in B. Arrowheads point to aggregate-like structures. Notice that these structures are positive only for PC but not for GFAP. (D) Mander's colocalization coefficient of GFAP and PC in B. (E, F) Quantification of the staining intensities of GFAP and PC, respectively, from images as shown in B. n = 5 in each group in D-F. (G) A schematic illustration of the spinal cord showing the regions of interest. (H) Quantification of PC-positive aggregate numbers from regions of interest as in G. n = 5 in control and 6 in ALS groups. (I) IHC of PC in subcortical white matter. The right

panels are enlarged views of the boxed areas in the left panels. Arrows point to astrocytes, and arrowheads point to aggregate-like structures. (J) Double IF staining for GFAP and PC in subcortical white matter. (K) Enlarged views of the boxed area in J. Arrowheads point to aggregate-like structures. (L) Mander's colocalization coefficient of GFAP and PC in J. (M, N) Quantification of staining intensity of GFAP and PC, respectively, from images as shown in J. (O) Quantification of PC-positive aggregate numbers from images as shown in J. $n = 4$ in control and 6 in ALS groups in L-O. Student t-test was used to compare ALS with controls, *$p < 0.05$, **$p < 0.01$.

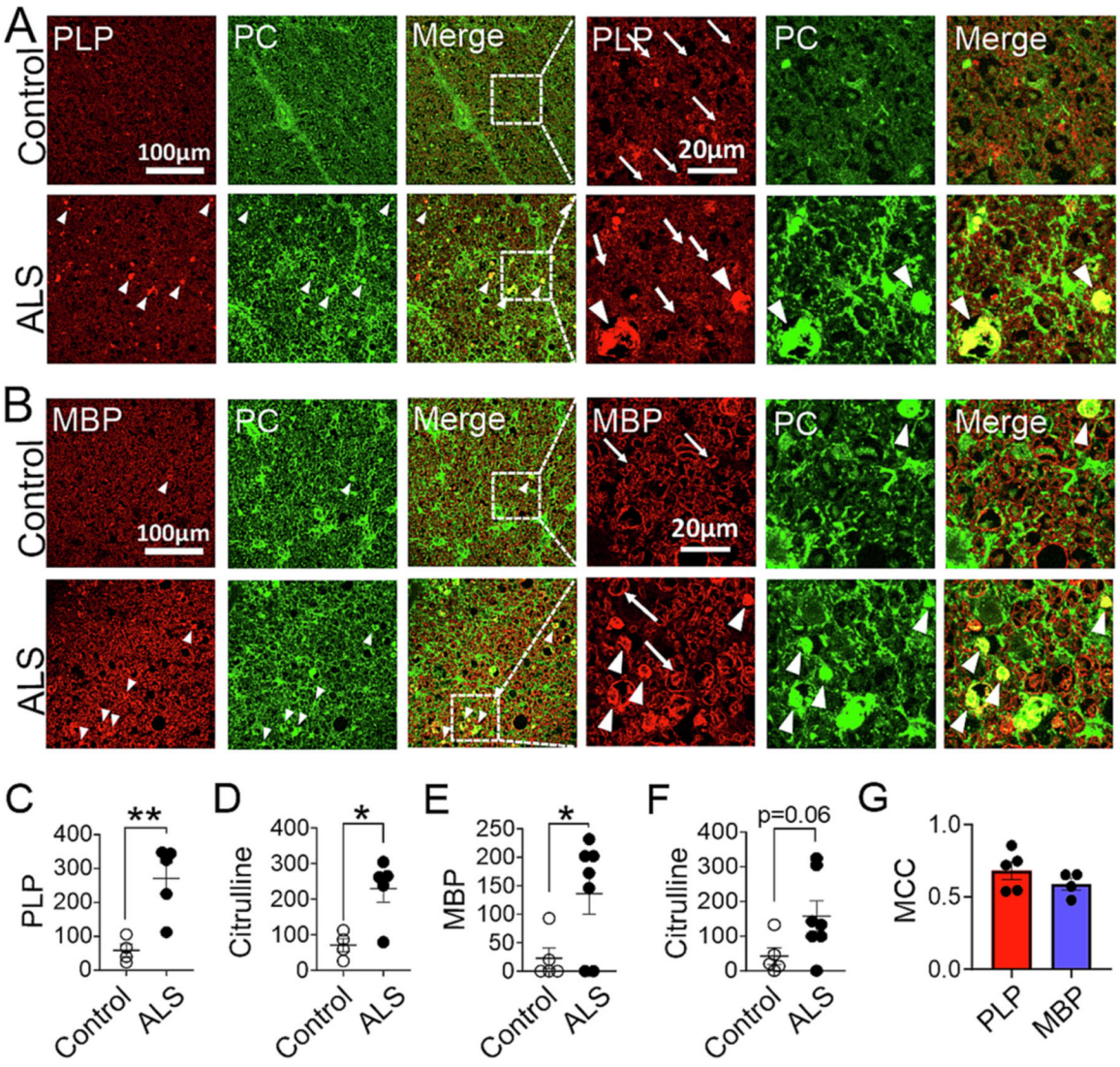

Fig. 8.

PC-positive aggregates colocalize with myelin proteins PLP and MBP in spinal cord white matter in ALS decedents. (A) Double IF staining for PLP and PC. Arrows point to ringlike PLP staining patterns. Arrowheads point to PLP and PC-positive aggregates. (B) Double IF staining for MBP and PC. Arrows point to ringlike MBP staining patterns. Arrowheads point to MBP and PC-positive aggregates. (C, D) Quantification of PLP and PC-positive aggregate numbers, respectively, from images as illustrated in A. n = 4 in control and 5 in ALS groups. (E, F) Quantification of MBP and PC-positive aggregate numbers, respectively, from images as illustrated in B. n = 5 in control and 7 in ALS groups. The numbers represent normalized numbers in 1 mm^2. (G) Mander's colocalization coefficient of PC-positive aggregates with PLP and MBP in ALS from images as illustrated in A and B. n = 5 in PLP and 4 in MBP groups. Student t-test was used to compare ALS with controls, *$p < 0.05$, **$p < 0.01$.

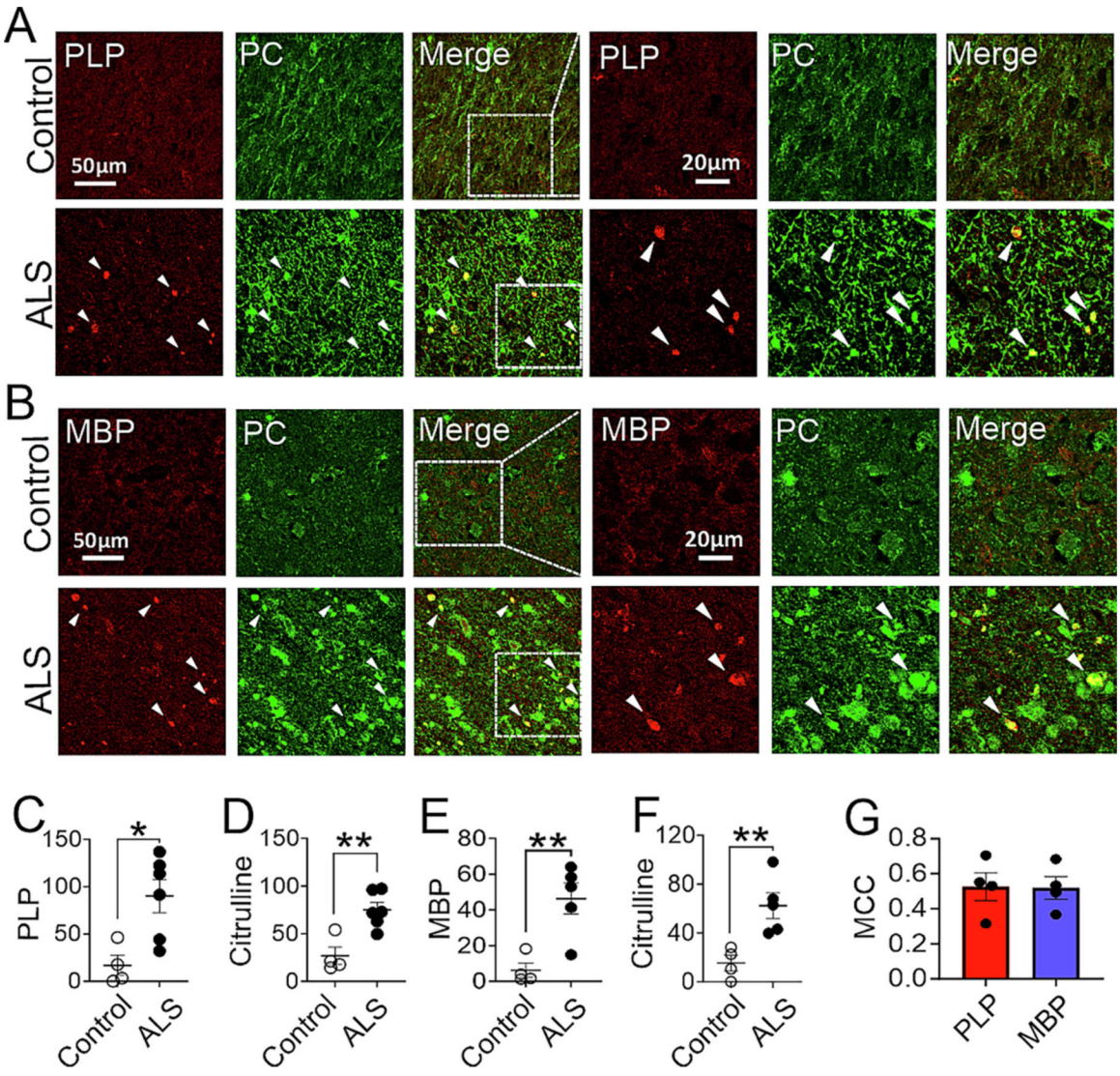

Fig. 9.

PC-positive aggregates colocalize with PLP and MBP in sub-motor cortex white matter in ALS decedents. (A) Double IF staining for PLP and PC in motor cortex subcortical white matter. Arrowheads point to PLP and PC-positive aggregates. (B) Double IF staining for MBP and PC in motor cortex subcortical white matter. Arrowheads point to MBP and PC-positive aggregates. (C, D) Quantification of PLP and PC-positive aggregate numbers, respectively, from images as illustrated in A. n = 4 in control and 6 in ALS groups. (E, F) Quantification of MBP and PC-positive aggregate numbers, respectively, from images as illustrated in B. n = 4 in control and 5 in ALS groups. The numbers represent normalized numbers in 1 mm^2. (G) Mander's colocalization coefficient of PC-positive aggregates with PLP and MBP in ALS from images as illustrated in A and B. n = 4 in each group. Student t-test was used to compare ALS with controls, *$p < 0.05$, **$p < 0.01$.

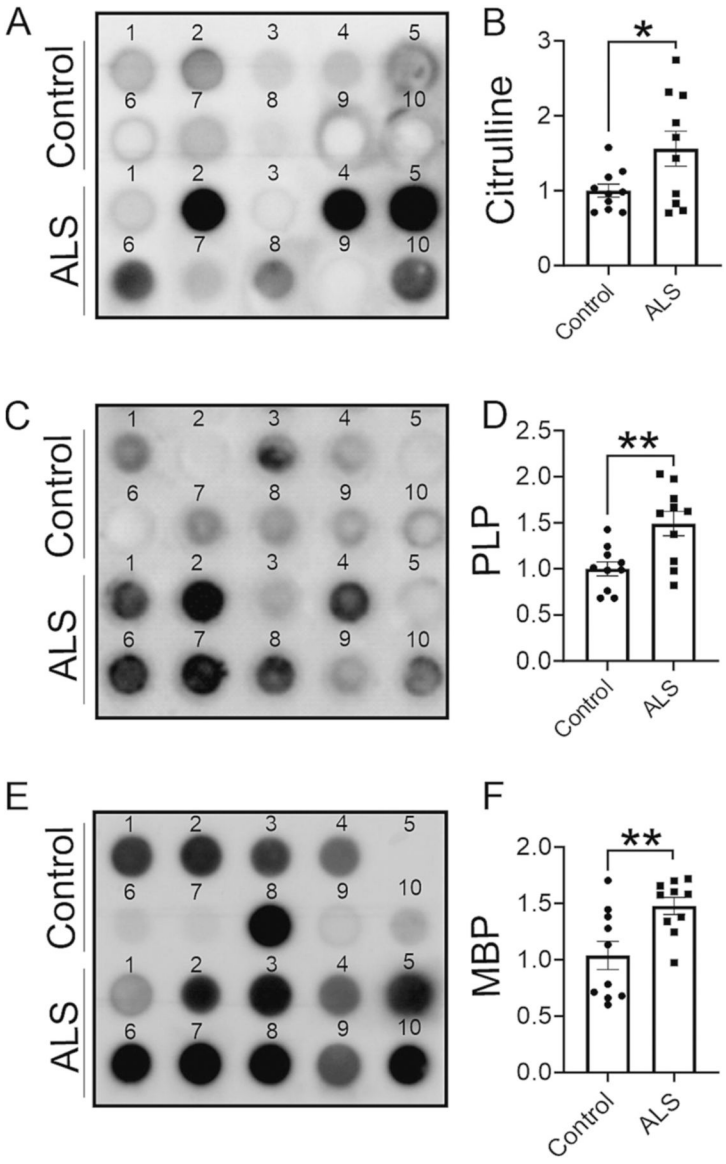

Fig. 10.

PC, PLP, and MBP are enriched in insoluble protein aggregates in the lumbar spinal cords of ALS decedents. Protein extracts from lumbar spinal cord tissues were assessed with filter trap assay for their protein aggregates and probed for (A, B) PC, (C, D) PLP, and (E. F) MBP. n = 10 in each group. Student's t-test was used comparing ALS with non-ALS controls. *$p < 0.05$, **$p < 0.01$. The panels are not intended to demonstrate correlation in individual samples because results are from experiments performed at different times, and the samples are not necessarily from the same decedents.